



Development and application of a hybrid terrain–multispectral image model of floodplain hydroperiod

S. M. Askew · Z. Munch · M. C. Grenfell ·
S. E. Grenfell

Received: 8 August 2024 / Accepted: 8 July 2025 / Published online: 20 July 2025
© The Author(s) 2025

Abstract Surface water mapping is a crucial aspect of studying river and wetland hydrological, geomorphological, and ecological processes. However, deriving inundation frequency solely from a normalised difference water index does not account for geomorphologically induced flooding dynamics, which reduces model accuracy. This study evaluated spatiotemporal inundation dynamics using a novel approach that combines geomorphologically relevant descriptors from a high-resolution LiDAR-derived digital elevation model with spectral outputs from Sentinel-2 imagery. The hydroperiod for the Nuwejaars River Floodplain was determined by: (1) mapping macro-scale geomorphic features and floodplain topography using a DEM and height above nearest drainage; (2) calculating the percentage of images (127 images with clouds < 20%), in which a particular pixel was flooded using Sentinel-2 imagery (2018 to 2023); (3) applying an unsupervised learning algorithm and thresholding in Google Earth Engine to

assign water frequency values to each pixel; and (4) deriving a hydroperiod that integrates geomorphic data and Sentinel-2 imagery to classify inundation patterns ($F1=0.67$, $n=60$). Accuracy assessment of the model, incorporating various spectral indices, was performed using a confusion matrix and validated against field data. The terrain-informed hydroperiod model achieved improved accuracy (75.9%), precision (66.7%), and recall (66.7%) statistics. Analysis revealed substantial spatial variation in inundation frequency closely related to floodplain geomorphology, with largest inundation frequencies occurring downstream of a partial avulsion and limited inundation in distal, abandoned channels. The study highlights the importance of integrating hydroperiod mapping with geomorphological insights. This approach is essential for understanding how historical and future changes in hydroperiod affect floodplain ecological processes and ecosystem service provision.

Supplementary Information The online version contains supplementary material available at <https://doi.org/10.1007/s11273-025-10072-1>.

S. M. Askew (✉) · Z. Munch · S. E. Grenfell
Department of Geography and Environmental Studies,
Stellenbosch University, Stellenbosch, South Africa
e-mail: stephanie@askewnet.co.za

M. C. Grenfell
Institute for Water Studies/Department of Earth Sciences,
University of the Western Cape, Bellville, South Africa

Keywords Surface water mapping · Inundation frequency · Remote sensing · Hydroperiod · Floodplain · Geomorphology · Wetland

Introduction

Surface water mapping is an invaluable component of research on river and wetland hydrological, geomorphological, and ecological processes (e.g., Khan et al. 2011), and an important monitoring focus

where ecosystem development is driven by changes in hydrology (Murray-Hudson et al. 2014). Remote sensing techniques provide practical and cost-effective means of investigating water and vegetation distributions over a variety of spatial scales (e.g., Huang et al. 2014; Jin et al. 2017; Pena-Regueiro et al. 2020), especially in regions that are data scarce or difficult to access, as also demonstrated by Murray-Hudson et al. 2014. These approaches support applications such as wetland ecosystem mapping and classification (e.g., van Deventer et al. 2022). Several active and passive sensors exist that are able to delineate the boundaries of inundated areas (and even detect changes in water level) where clouds, trees or other objects do not obscure water surfaces. Although temporal trend mapping has lagged behind analyses of spatial variation, this is changing due to the increased availability of multitemporal imagery, driven by the rising number of satellite missions, improvements in spatial and temporal resolution, and open-access data policies adopted by programs such as Landsat and Sentinel.

These advancements allow us to address critical questions around responses in river and wetland inundation to changes in climate in both the short (e.g., an individual drought) and longer-term (e.g., rainfall variation due to natural climatic oscillations and/or anthropogenic climate change). For example, significant changes in inundation area may occur due to climate change, which has implications for ecosystem persistence, structure and function, and for ecosystem service provision (Kordelas et al. 2018). The ability to map and monitor such changes is vital in adapting to, or mitigating their impacts, and in developing management or rehabilitation programmes (Wu and Liu 2014), thereby engaging researchers, policymakers and those involved in restoration, drought and flood management, conservation, land-use planning, and climate change mitigation strategies (Wu and Liu 2015).

In wetland science especially, characterising variation in the frequency and duration of inundation (the hydroperiod; Foti et al. 2012; Tockner and Stanford 2002) is critical to understanding ecosystem structure, function, and dynamics (Jin et al. 2017; Murray-Hudson et al. 2014). In floodplain wetlands, inundation patterns may be defined both spatially (i.e., the area of land inundated) and temporally (i.e., the intra- and inter-annual frequency of inundation). These patterns are a function of several interacting controls,

including (i) the hydrological regime of the river channel(s) bringing water into the floodplain, (ii) the discharge capacity of the channel(s) (i.e., how much water they can hold before spilling to the floodplain surface), (iii) the morphology of the floodplain surface, (iv) the infiltration capacity of the floodplain surface, (v) antecedent (pre-flood) inundation extent, and (vi) post-flood atmospheric water demand (evaporation). Floodplain surface inundation can occur if inflows exceed the discharge capacity of the floodplain channel(s) (controls i and ii), or in some cases without channel spilling if local rainfall exceeds the infiltration capacity of the floodplain surface (controls iv, v and vi). These controls are primarily shaped by climate and catchment processes, whereas floodplain water and sediment dispersal patterns and inundation duration are further influenced by the morphology and composition of the surface (controls iii and iv; Meyerhoff and Dehnhardt 2007).

Floodplain geomorphology, including the arrangement of, and distances between, main channels and abandoned channels, and the configuration of geomorphic units such as oxbow lakes creates preferential flow paths and gradients that govern the way water and sediment move and accumulate across the surface, spatially and temporally (Pereira et al. 2021). The diversity in geomorphic units, spatio-temporal variation in hydrology, and distinctive physiochemical environments (Ellery et al. 2011) combine to make floodplains one of “the most biologically productive and diverse ecosystems on earth” (Tockner and Stanford 2002, p. 308). This template of diversity is an essential parameter governing the provision of ecosystem services (Kordelas et al. 2018).

As such, insights into the spatiotemporal pattern and dynamics of river and floodplain inundation constitute a-priori understanding for wetland management and conservation. For example, hydroperiod mapping helps to identify areas that are suitable for specific hydrophytic vegetation, waterbirds, and other species, assess habitat availability, and understand lateral and longitudinal hydrological connectivity (Uhlemann et al. 2016). The collection of this hydrological information greatly aids wetland conservation and restoration efforts by informing restoration plans that aim to reinstate hydrological connectivity similar to a reference site (e.g., a historical, undisturbed hydroperiod), and/or measuring restoration success (Hua et al. 2016; McCormack et al. 2023).

Furthermore, hydroperiod mapping can provide a detailed indication of the spatial extent and degree of provision of ecosystem services such as flood attenuation, nutrient assimilation, carbon sequestration, sediment trapping, and pollutant immobilisation (Acreman et al. 2007). While previous studies have focused on developing an understanding of spatio-temporal variation in wetland inundation (e.g., Khan et al. 2011; Kordelas et al. 2018; Smith 1997; Wu and Liu 2015), few have integrated the inundation record with insights of floodplain geomorphology. Furthermore, integrating LiDAR-derived HAND models with multispectral time series data is a replicable approach for other hydroperiod studies.

Recent advances in aerial survey technologies have greatly enhanced our ability to map and understand floodplain geomorphology. High-resolution LiDAR data and spatial resolution imagery, such as 8 cm orthophotos, now allow for the precise delineation of geomorphic features, including subtle elevation changes and abandoned channel forms that were previously difficult to identify. When these detailed terrain datasets are integrated with satellite-based monitoring of surface water dynamics, such as hydroperiod mapping from multitemporal Sentinel-2 imagery, they enable a more comprehensive assessment of how geomorphology influences inundation patterns.

These broader integrated insights are necessary to evaluate the implications of historical spatial variation and future changes in hydroperiod for floodplain ecological processes and ecosystem service provision. To address this gap, we evaluated the spatiotemporal pattern and dynamics of inundation in relation to geomorphology for a floodplain of the Nuwejaars River near Cape Agulhas, South Africa. Macro-scale geomorphic features within the floodplain were delineated from (i) topographic information extracted from a 0.5 m ground surface digital elevation model (DEM), derived from a high-resolution LiDAR survey point cloud, and (ii) 8 cm resolution colour orthorectified imagery. The primary aim of the study was to evaluate how geomorphological characteristics influence the spatial and temporal variability of inundation.

To analyse and map the spatiotemporal variation in inundation of the Nuwejaars River floodplain surface between 2018 and 2023, an unsupervised learning model was developed on Sentinel 2 satellite imagery in Google Earth Engine. Various combinations of

spectral bands and DEM-derived layers were tested against field samples to select the best hydroperiod model. This hybrid terrain–multispectral image model was used to characterise and compare the hydroperiod for delineated macro-scale environments across the floodplain, and to explain differences in the frequency of inundation across the floodplain related to floodplain geomorphology.

Study area

The study area is a floodplain wetland (34° 39' 50.31" S, 19° 54' 31.12" E) located on the Wiesdrif farm along the Nuwejaars River, and is situated on the Cape Agulhas coastal plain, 160 km southeast of Cape Town, in the Overberg region of the Western Cape, South Africa (Fig. 1). The Nuwejaars River is a non-perennial river with a catchment area of 760 km², located in the greater Heuningnes Catchment (McLachlan and Burns 1992; Seaton et al. 2020). The Nuwejaars River Floodplain has an areal extent of 12.24 km², and the river's main tributaries include the Jan Swartskraal, Koue, Boskloof, Wolwegatskloof, Pietersilieskloof and Uintjieskriol rivers (Bickerton et al. 1984). The headwaters of the Nuwejaars River originate northwest of the town Elim, in the Bredasdorp mountains. It flows in a southeasterly direction and begins to meander as it reaches the low-gradient Agulhas Plain lowlands, forming a series of riparian wetlands, such as the seasonal Nuwejaars meandering river floodplain wetland (Jagganath 2021).

The Nuwejaars River catchment's climate type, according to the Köppen classification, is a 'warm summer Mediterranean climate', characterised by wet, cool winters and dry, hot summers (Kottek et al. 2006). The catchment's mean aridity index, calculated from mean annual precipitation and mean annual evapotranspiration ratios (Trabucco & Zomer, 2018), is 0.44 which corresponds to a semi-arid climate, and thus a dryland environment. The coastal region of the Agulhas Plain receives 450 mm of rain per annum and the foothills further north receive 650 mm per annum on average (Erasmus 2013; Privett et al. 2014). Seventy percent of the rainfall occurs during the austral winter months, resulting in the period between June and August receiving approximately 50 to 55 mm per month (Khungwayo 2022; Privett et al. 2014). Precipitation in the Western Cape

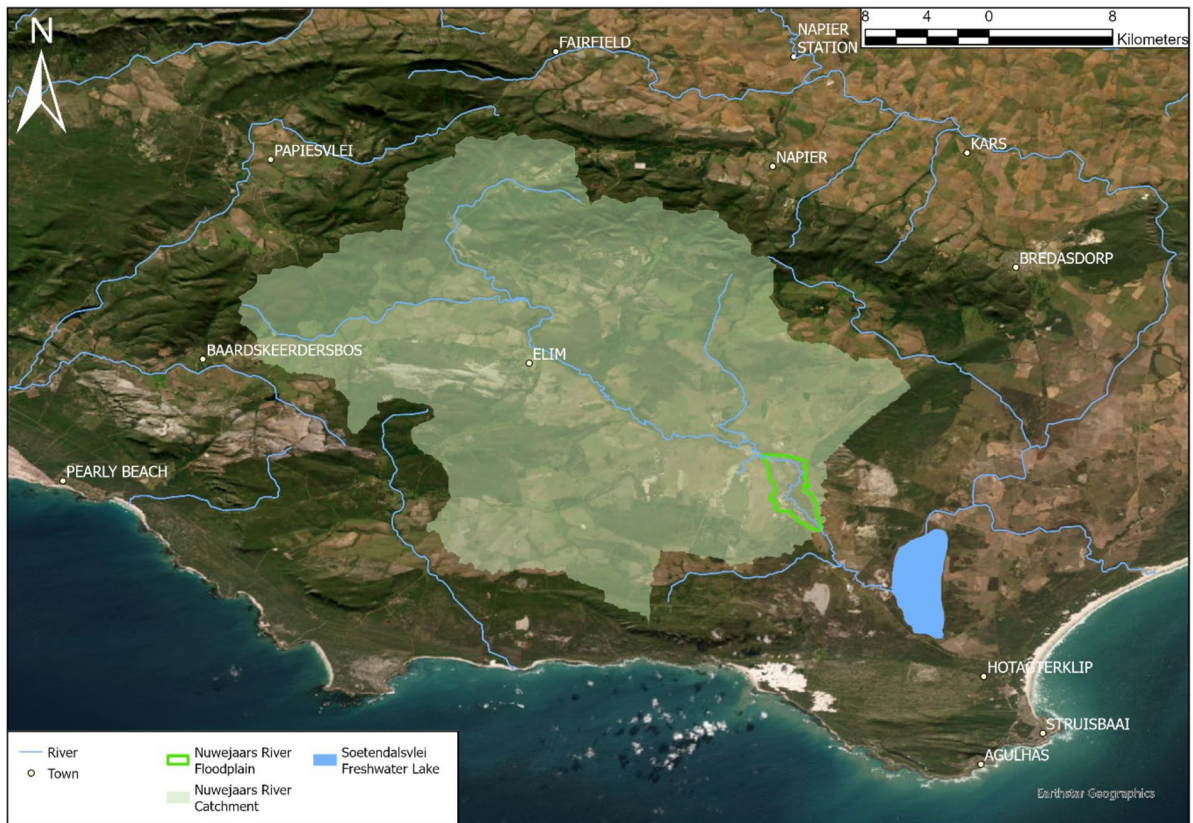


Fig. 1 Study area map of the Nuwejaars River Floodplain wetland and its catchment, with Soetendalsvlei and major rivers presented. The watershed tool in ArcMap (version 10.8.1) was

applied to Stellenbosch University's 5 m DEM (SUDEM) to extract the catchment area upstream of the study area

is predominantly associated with the passing of cold fronts associated with mid-latitude cyclones and cut-off lows. The mean annual temperature, according to Schulze (1997), is 16.9 °C.

The Nuwejaars River has its highest flows during August, after the wet winter season, and experiences little to no flow in the summer months between October and April (Seaton et al. 2020). From November to March, potential evaporation exceeds precipitation (Kraaij et al. 2009), and periods of no or low flow enable vegetation to grow within the channel (Jagganath 2021). The wetland appears to be in a transitional state, whereby it displays meandering river floodplain characteristics (Grenfell et al. 2019), but the primary channel is undergoing an avulsion.

Downstream of the floodplain, the Nuwejaars River enters Soetendalsvlei (Fig. 1), a large (20 km²), shallow, inland, coastal freshwater lake (Gordon et al.

2012). This lake spills through a channel to join the Kars River, which becomes the Heuningnes River after this confluence. The Heuningnes River enters the Indian Ocean at De Mond, a Ramsar wetland of international importance (Jagganath 2021).

The Agulhas coastal plain is a relic of a 'wave-cut platform' which was formed as a result of a series of transgressions in the mid-Miocene and mid-Pliocene periods (Kraaij et al. 2009). Tertiary-age calcareous sands primarily cover the Agulhas Plain. The coastal mountains of the catchment, such as the Koueberge, Normanskop and Soetmuisberg, are comprised of Table Mountain Group (TMG) sandstone forming part of the Cape Fold Belt which, in some sections, are limestone capped (Thwaites 1987). Bokkeveld Group shale 'undulating plains' are found at the foothills of these mountains, with both forming part of the Cape Supergroup (Kraaij et al. 2009). Paleozoic

sediments, from the Cape Supergroup, primarily underlie the Agulhas Plain (Kraaij et al. 2009). The TMG and Bokkeveld Groups overlie the Cape Granite Suite and Malmesbury Group basement rocks (Jagganath 2021). Dominant floodplain sediments are clastic, while wetter backswamp environments, oxbows and paleochannels tend to have greater organic content. Groundwater in this catchment is stored in secondary aquifers of the TMG and Bokkeveld Group and in a primary aquifer of the Bredasdorp Group lithology (Khungwayo 2022).

The region falls within the Cape Floral Kingdom, home to Overberg Sandstone Fynbos (covering almost 55% of the Agulhas Plain), Limestone Fynbos, Ferricrete Fynbos and highly threatened lowland fynbos (Mucina and Rutherford 2006; Privett et al. 2014). Within most of the wetlands found on the Agulhas Plain, restioids are the most common vegetation type (Kraaij et al. 2009). Large portions of the catchment is used for cattle and sheep pastures and cultivation of crops (such as wheat and canola), while the remainder is natural fynbos within wildlife conservation zones (Erasmus 2013). Livestock, grain, and dairy farming are prominent around the Nuwejaars River Floodplain, which is used for rotational grazing. A dairy farm is located at the southern end of the floodplain. Wetlands across the region are increasingly threatened by agricultural expansion and infrastructure development, yet there remains limited understanding of how these systems respond to hydrological variability driven by both natural processes and anthropogenic influence. This study provides a foundation for developing the insight needed to inform future wetland management on the Agulhas Plain.

Materials and methods

Materials

The aerial LiDAR survey of the floodplain study area was conducted by Southern Mapping Geospatial (Pty) Ltd on 27 April 2022, using an Optech Orion M300 (12SEN306) LiDAR scanner with ground-control points to provide detailed, high-resolution topography at 8 cm resolution. A 0.5 m ground surface digital elevation model (DEM) of the wetland was created

from the LiDAR data using the LAS dataset tool in ArcGIS Pro version 3.0.2.

Fieldwork was undertaken between the 1st and 4th of October 2022 to acquire ground truth data. In-field water level measurements were taken at 58 sites using a Trimble GeoXH DGPS for spatial accuracy (10–30 cm). These sites were located along eight transects orientated across the width of the floodplain, which captured the macro-features that were identified in the desktop and image analysis, as well as longitudinal and cross-sectional transitions within the floodplain system. The water level measurements represent ground-truth data.

The Harmonised Sentinel-2 Level 2A Surface Reflectance (SR) product obtained from the GEE public data catalogue was used. Sentinel-2 imagery is freely available and has a finer spatial (10 m) and temporal (5 days) resolution than other freely available imagery, such as Landsat, and it has proved useful in determining inundation patterns in previous studies (e.g., van Deventer et al. 2022). 127 Sentinel-2 images, with cloud cover less than 20% (selected using the GEE filter function), were used in the model from 22/12/2018 to 21/12/2023 (all dates displayed in Supplementary Table S1). There is a reasonably even temporal distribution across months, seasons, and years, averaging 25 images per year (and 10 images per month in total), though 2018 has only a single image and 2021 had fewer images available for use compared to other years.

Methods

The floodplain topography and morphology were described via geomorphic mapping of macro-scale features based on their relative elevation and form. The identification/delineation and digitisation of these features were accomplished using the terrain metric, height above nearest drainage (HAND), derived from a 5 m resolution LiDAR DEM. The features were distinguished by their relative elevation to the current channel and changes in gradient, and accordingly divided into various backswamp environments. Backswamps, in geomorphology, represent a depositional, usually inward-draining feature often found on a floodplain's surface. Other macro-features mapped included the current channel and the abandoned course with their associated alluvial ridges.

HAND was calculated from the DEM and the stream network, based on the workflow of Garousi-Nejad et al. (2019). For all cells in the DEM, the vertical distance to the nearest stream was computed using the open-source software TauDEM (Tarboton 1997) and vector/raster manipulations using GDAL/OGR in Python. Flow direction was determined using the D-Infinity method, and the distance from each cell to the nearest stream computed along the flow paths.

Using remote-sensing techniques and available Sentinel-2 imagery, the method for determining the spatial variation in inundation of the floodplain involved calculating the percentage of time that a particular pixel was flooded in imagery from 2018 to 2023. All computational steps were completed in Google Earth Engine (GEE) using the JavaScript editor, producing a ready-to-use product without manually processing very large and numerous geospatial datasets.

An unsupervised machine learning approach was developed (Wu et al. 2019) and validated against inundation field data. K-means clustering is a type of unsupervised learning wherein data points are grouped into different sets based on their similarity with “K” signifying the number of classes (Xie et al. 2008). The GEE clusterer algorithm used implements K-means clustering, based on the algorithms with the same name in Weka data mining software (Frank et al. 2016), which aims to find the best division of n entities into k groups (called clusters). The total distance between the group members and corresponding centroid is minimised, with each entity belonging to the cluster with the nearest mean. Clusters are labelled based on the JRC Water threshold. Spectral indices and DEM-derivatives (Slope, HAND) were selected as features in the hydroperiod model to find the optimal band combination with the highest accuracy compared to the field data.

Commonly used spectral indices for wetland analysis are the Normalised Difference Vegetation Index (NDVI) and the Normalised Difference Water Index (NDWI) (Wu et al. 2019). The most frequently used NDWIs include (1) the $NDWI_{G/NIR}$ (McFeeters 1996), (2) the $NDWI_{NIR/MIR}$ (Gao 1996), and (3) the modified NDWI (Xu 2006). Campos et al. (2012) evaluated these three NDWI indices finding that they perform differently in detecting seasonal and permanent water. They found that $NDWI_{G/MIR}$ and $NDWI_{NIR/MIR}$ were effective in identifying permanent and seasonal

water bodies, respectively, whereas $NDWI_{G/NIR}$ performed poorly, missing most water features (Campos et al. 2012). Therefore these NDWI indices were tested along with additional indices used for automatic water extraction (Table 1) and applied to distinguish water maps with seasonal and permanent features that might be missing in simple mapping of aquatic systems.

Unsupervised classifications are often used in thematic mapping applications, as they automatically transform raw data into practical information based on spectral pixel-based statistics (Xie et al. 2008). In Wu et al.’s (2019) analysis, six clusters were recommended. This number seemed appropriate given that the goal of the final output was binary (i.e., either presence or absence of surface water). Nevertheless, a few different cluster inputs were applied and the output visually inspected against aerial photography in conjunction with field knowledge. Six clusters most accurately represented the field site. For an initial test as to whether the clusters were valid, the outputs were compared to the European Commission Joint Research Centre (JRC) Global Water Occurrence product (30 m). Inundated clusters were identified from the JRC water dataset (Pekel et al. 2016) with a threshold of 50% water occurrence between 1984 and 2023 (Wu et al. 2019). A thresholding algorithm (Huang et al. 2014) was used to select the 90th percentile (50%) from the JRC water dataset, which had a maximum value of 65 for the study area. For a cluster to be classified as inundated, the area of the cluster had to exceed 30% of the pixels. Testing of the outputs indicated that the model was fairly insensitive to the threshold, setting the threshold to slightly larger or lower than 30% made very little observable difference to areas mapped as inundated. As such, we followed the method suggested by Wu et al. (2019).

An accuracy assessment was performed using a confusion matrix representing counts from predicted and actual values. A true positive (TP) is an outcome where the model correctly predicts the positive class, while a true negative (TN) is where the model correctly predicts the negative class. Accuracy, Precision, Recall, and F1 Score are key performance metrics for evaluating machine learning models to provide quantitative assessments of a model’s predictive capabilities. Precision ($TP/(TP+FP)$) evaluates positive prediction quality. Recall assesses sensitivity to positive instances ($TP/(TP+FN)$). F1 Score shows the

Table 1 Selected spectral indices tested against field data to identify areas of inundation

Index	Formula	Target	References
Normalised Difference Vegetation Index (NDVI)	$\frac{(NIR-R)}{(NIR+R)}$	Vegetation density and health	Tucker (1979) Liu and Huete (1995)
Normalised Difference Water Index (NDWI or NDWI _{G/NIR})	$\frac{(NIR-G)}{(NIR+G)}$	Detection of water	McFeeters (1996)
Modified Normalised Difference Water Index (mNDWI)	$\frac{(G-SWIR1)}{(G+SWIR1)}$	Enhanced extraction of open water bodies	Xu (2006) Han-Qiu (2005)
Revised Normalised Difference Water Index (rNDWI)	$\frac{(G-R)}{(G+R)}$	Extraction of water-land boundary	Cao et al. (2008)
Normalised Difference Moisture Index (NDMI or sNDWI or NDWI _{NIR/MIR})	$\frac{(NIR-SWIR2)}{(NIR+SWIR2)}$	Vegetation water content	Gao (1996)
Modified Soil Adjusted Vegetation Index (MSAVI2)	$(2NIR + 1 - \sqrt{(2NIR + 1)^2 - 8(NIR - R)})/2$	Enhance vegetation monitoring in areas where soil is visible	Qi et al. (1994)
Water in Wetlands (WIW)	NIR < 0.1804 AND SWIR1 < 0.1131	Presence of water in wetlands	Lefebvre et al. (2019)
Automated Water Extraction Index (AWEI)	AWEI(SH) = B + 2.5*G - 1.5*(NIR + SWIR1) - 0.25*SWIR2 (scenes with shadows labelled AWE1) AWEI(NSH) = 4*(G-SWIR2) - (0.25*NIR + 2.75*SWIR1) (scenes without shadows labelled AWE2)	Classifying land cover into binary water and non-water categories	Feyisa et al. (2014)

Sentinel-2 bands: B=Blue (B2); G=Green (B3); R=Red (B4); All bands=B*; NIR=Near Infrared (B8); SWIR1=(B11); SWIR2=(B12)

balance between precision and recall (Kulkarni et al. 2020), while accuracy measures overall correctness.

True values from the hydroperiod model applied to a Sentinel-2 image taken on the 2nd of October were validated using in-field water level measurements taken between 1 and 4 October 2022. Measurements were taken at 58 sites using a Trimble GeoXH DGPS for spatial accuracy (10–30 cm). Twenty one of the sites were classified as being inundated (water level > 1 cm) on that day, allowing wet and dry pixels to be classified based on the field samples. The confusion matrix was based on a total of 58 validation sites, of which 21 were classified as wet and 37 as dry. Seventeen different combinations of bands and indices (Table 1) were tested to determine the most accurate model. For each one of the different combinations, the true positive, false positive, true negative, and false negative were calculated to compare the accuracy, precision, and recall of each. Precision is defined as user accuracy and recall as producer accuracy.

Using the optimal model, all available Sentinel-2 images from 2018 to 2023, with a cloud cover

of less than 20%, were selected for processing. The selected spectral indices (Table 1) were calculated for each image in the image collection stack and added along with the slope and HAND computed from the LiDAR DEM, resulting in a multi-temporal 19-band image collection used for unsupervised classification. Inundation was predicted for each image (date) in the image collection (127 images with clouds < 20%), signified by a 1 for inundation and a zero for no inundation. The classified time series was summarised and the percentage inundation was computed from the total number of images selected.

In South Africa, hydroperiod classes (sensu Ollis et al. 2013, 2015) are used to define the inundation period of wetlands (defined in Table 4). The hydroperiod classes developed by Ollis et al. (2013, 2015) correspond to a one-year timeframe but should be considered over a longer period and can therefore be generalised to the longer-term dataset presented here.

The pattern of inundation and differences in the frequencies across the floodplain were explained by including geomorphic and topographic information. The analysis of both the hydroperiod and the

morphology of the floodplain was used to provide insights into the sedimentation patterns of the system.

Results

Accuracy assessment

The seventeen different combinations of bands and indices used to determine the most accurate model when compared with field measurements can be found in Table 2. The true positive, false positive, true negative, and false negative, accuracy, precision, and recall of each combination is shown.

The confusion matrix revealed varying levels of accuracy for different index combinations (Table 2). The highest accuracy (75.9%) was achieved with combination 7, which included all bands (B.*), NDVI, NDWI, RNDWI, MNDWI, SNDWI, slope, and HAND. Several combinations tied for the second-highest accuracy (74.1%), including combinations 6, 9, 12, 14, 15, and 16. The lowest accuracy (43.1%) was observed with combination 3, which used only B2, B3, B4, B8, B8A, NDWI, and NDVI.

The highest precision (85.7%) was achieved by combination 8, which included additional indices like WIW, AWE1, and AWE2. However, this combination had a low recall (28.6%). The highest recall (66.7%) was observed in combination 7, which also had the highest accuracy, and was therefore selected for the analysis. Combinations 2 and 3 had zero precision and recall, indicating poor performance in detecting inundated areas.

Floodplain geomorphology

The HAND model was used to differentiate portions of the floodplain with similar elevation into macro-scale features (Fig. 2), including various backswamp environments that make up the surface area of the floodplain, as well as the current channel and the abandoned channel with their associated alluvial ridges.

The macro-features, determined with HAND, as well as the location of the partial avulsion (range of 1.25 to 3.19 m; Fig. 2B), determined by visual mapping, are displayed in Fig. 3A, along with the locations of nine cross-sections (Fig. 3C). The different floodplain macro-features were grouped into upper,

Table 2 Confusion matrix for the 17 different index combinations that were tested. A variety of individual bands, as well as vegetation and water indices were applied in conjunction with

selected terrain derivatives considered important in terms of inundation patterns (e.g., slope and HAND)

No	Band/layer combinations	TP	FP	TN	FN	Accuracy	Precision	Recall
1	B.*,ndwi,ndvi	11	8	29	10	0.690	0.579	0.524
2	B2,B3,B4,B8,ndwi,ndvi	0	3	34	21	0.586	0	0
3	B2,B3,B4,B8,B8A,ndwi,ndvi	0	12	25	21	0.431	0	0
4	B.*,ndwi,ndvi,mndwi	12	7	30	9	0.724	0.632	0.571
5	B.*,ndwi,ndvi,rndwi	11	9	28	10	0.672	0.55	0.524
6	B.*,ndwi,ndvi,rndwi,mndwi	13	7	30	8	0.741	0.65	0.619
7	B.*,ndvi,ndwi,rndwi,mndwi, sndwi, slope,hand	14	7	30	7	0.759	0.667	0.667
8	B.*,ndvi,ndwi,rndwi,mndwi,sndwi, slope,hand,wiw,awe1,awe2	6	1	36	15	0.724	0.857	0.286
9	B.*,ndvi,ndwi,rndwi,mndwi,sndwi, slope,hand,msavi2,awe1,awe2	13	7	30	8	0.741	0.650	0.619
10	B2,B3,B4,B8,B8A,B12,ndvi,ndwi, rndwi,mndwi,ndwi,slope,hand, msavi2,awe1, awe2	13	8	29	8	0.724	0.619	0.619
11	B.*,ndvi,rndwi,slope,hand	13	8	29	8	0.724	0.619	0.619
12	B.*,ndvi,rndwi	13	7	30	8	0.741	0.650	0.619
13	B.*,ndvi,mndwi	12	7	30	9	0.724	0.632	0.571
14	B.*,ndvi,sndwi	12	6	31	9	0.741	0.667	0.571
15	B.*,ndwi,ndvi,rndwi,mndwi,slope, hand	13	7	30	8	0.741	0.650	0.619
16	B.*,ndvi,rndwi,msavi2	13	7	30	8	0.741	0.650	0.619
17	B.*,ndvi,rndwi,msavi2, slope, hand	12	9	28	9	0.690	0.571	0.571

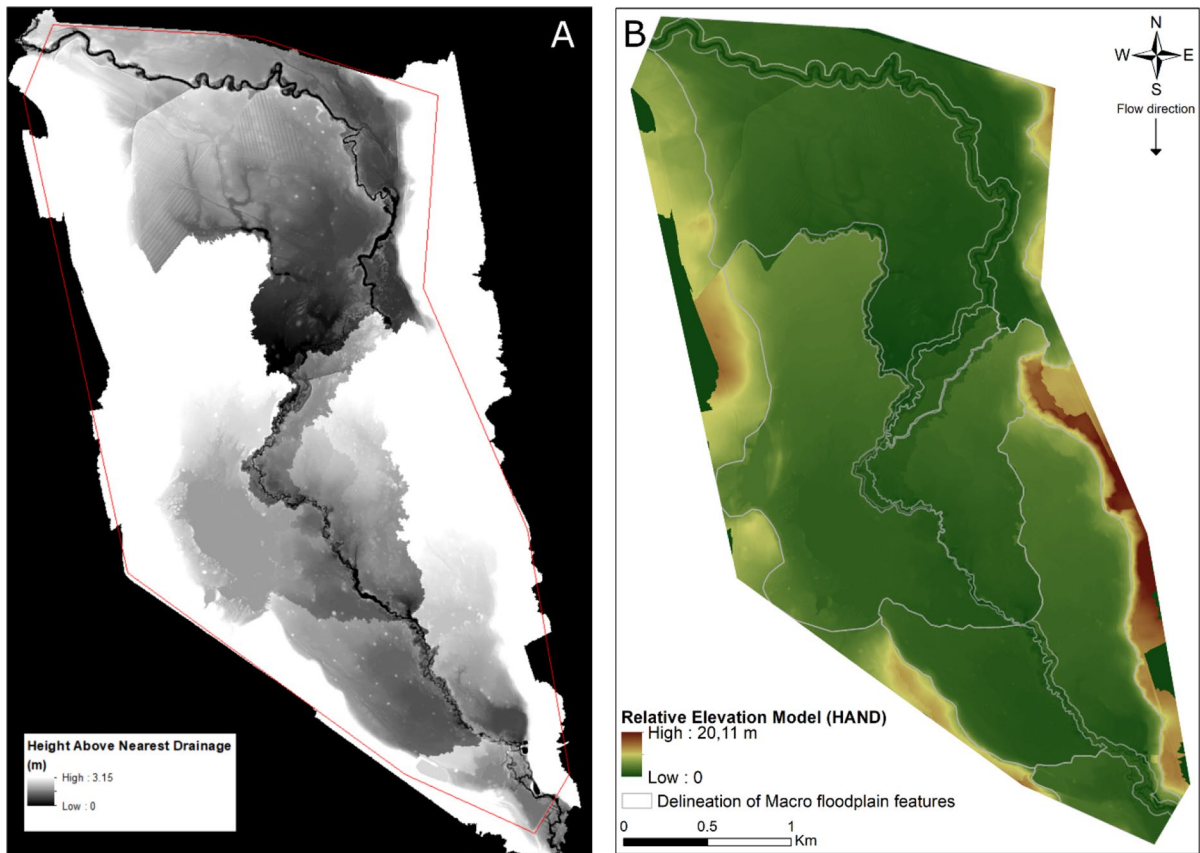


Fig. 2 **A** The HAND model result, **B** The HAND model imported into ArcMap to be used as a Relative Elevation Model (REM) and used to delineate macro-features by their differing relative elevations

central, and lower backswamps, and are indicated on the longitudinal profile (Fig. 3B). The floodplain has an overall mean slope of 0.05%, the upper portion is very gently sloped (0.005%), steepening toward the central (0.09%) and lower backswamps (0.11%).

Table 3 demonstrates the area and mean relative elevations (from the HAND model) in reference to the current channel and actual elevations of each macro-feature. Moving from upstream to downstream of the floodplain, the actual elevation values (from the DEM) show a decreasing trend, as expected. The lower east backswamp has the highest mean relative elevation (REM) (Table 3), which can be accounted for by the observation that this area of the floodplain is confined by a steep embankment that leads to a farm road.

The central lower backswamp has the lowest mean relative elevation (Table 3). It is located between the alluvial ridges of both the current channel and the

abandoned channel (depicted in Fig. 3A). The central upper backswamp has the second lowest mean REM value. This macro-feature starts where the incomplete avulsion occurs (shown in Fig. 3A), and is bound by two channels on either side, with the new channel establishing itself to the east and the old channel, which only flows during periods of higher discharge, to the west. The new channel has not established itself long enough to create an alluvial ridge, which is why the 'current channel and alluvial ridge' feature is still depicted to the west (Fig. 3C, cross-section 3).

The east and west sides of the floodplain (separated by the current channel) are elevated somewhat differently. Generally the eastern backswamp environments have a slightly higher mean relative elevation compared to the western backswamps (Table 3). The exception is the central east and west backswamps, in which the central west backswamp has a slightly higher mean elevation. The differences in elevation

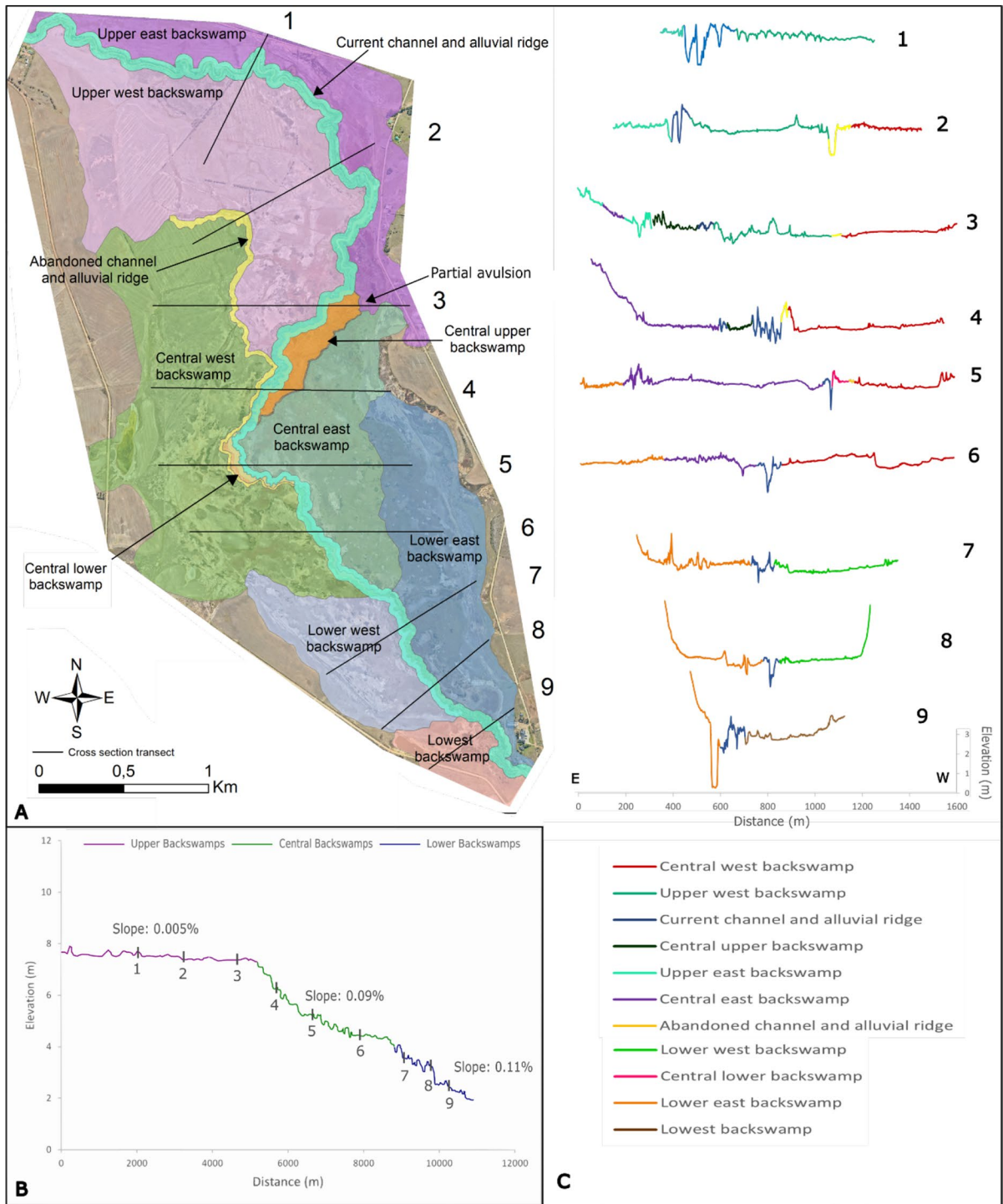


Fig. 3 **A** Locations of cross sections across the Nuwejaars River Floodplain. The macro-scale floodplain features are delineated, coloured and labelled on the map. The location of the partial avulsion is marked by an arrow. **B** Valley longitudinal profile of the Nuwejaars River Floodplain, with upper, cen-

tral and lower macro-features and their corresponding slopes indicated. **C** Cross-sections across the Nuwejaars River Floodplain orientated perpendicular to the current channel from east to west

Table 3 The area, mean relative elevation (REM) (derived from the HAND model), and the mean digital elevation model (DEM) of each macro-feature. Macro-features arranged from upstream to downstream

Macro-features	Area (km ²)	REM (m)			DEM (m)		
		Min	Max	Mean	Min	Max	Mean
Upper east backswamp	0.87	0	8.58	2.26	7.31	14.94	9.69
Upper west backswamp	1.92	0	7.68	1.82	6.53	13.92	8.85
Current channel and alluvial ridge	0.15	0	4.86	1.28	0.85	11.37	7.09
Abandoned channel and alluvial ridge	0.09	0	4.91	1.69	4.81	9.29	7.6
Central upper backswamp	0.15	0.15	3.12	1.74	6.33	8.95	7.45
Central west backswamp	2.00	0.74	7.58	2.77	4.67	11.96	7.12
Central east backswamp	0.89	0	7.43	2.23	4.5	11.81	6.74
Central lower backswamp	0.02	0	2.95	1.2	4.98	8.21	6.39
Lower east backswamp	1.01	0	9.22	2.92	0.9	11.93	6.13
Lower west backswamp	0.63	0	7.45	1.67	3.95	11.3	5.52
Lowest backswamp	0.30	0	5.24	2.45	2.67	7.95	5.11

explain why some of the macro-features may be substantially wetter than others.

The central west backswamp is the largest macro-feature, spanning 2 km², with the upper west backswamp and lowest east backswamp following as the next largest macro-features. The central lower backswamp is the smallest (0.02 km²) and relatively lowest macro-feature. The abandoned channel with its alluvial ridge macro-feature has the second smallest area (0.09 km²). The central upper backswamp, as well as current channel and alluvial ridge, are also small macro-features with an area of 0.15 km² each. As shown in Fig. 3A, both the central upper and lower backswamps are confined by a channel (either active or abandoned).

Frequency of inundation

Areas of frequent inundation (greater than 20%) are largely confined to the channel region in the proximal portion of the floodplain (Fig. 4A). The channel loses confinement at the partial avulsion (labelled in Fig. 3A), at which point flood waters spread laterally and diffuse flows occur throughout this region of the floodplain, which leads to larger areas within this section of the floodplain being flooded more often. Table 4 shows the area and percentage of the floodplain extent (%) within each inundation frequency class categorised according to Ollis et al. (2013, 2015).

According to the hydroperiod classes of Ollis et al. (2013, 2015), shown in Fig. 4B, most of the floodplain (91.64%) was intermittently inundated

over the five years and 7.82% of the floodplain was seasonally inundated (Table 4). An area is permanently inundated if it is inundated more than 75% of the time (Ollis et al. 2013, 2015), with only 0.33% of the floodplain permanently inundated. According to the hydroperiod model, 0.20% of the floodplain was never inundated over the five years. These areas occur at the top of the floodplain, mainly in the upper-west backswamp environment.

Hydroperiod of the macro-features

When considering the macro-features by hydroperiod, it becomes apparent that over the five-year study period, flooded areas are concentrated in the central and lower portions of the floodplain (Fig. 4A and Table 4), with the upper portions remaining relatively dry throughout the year. As such, the central east backswamp has the highest mean inundation frequency (18.30%), while the upper west backswamp has the lowest mean (8.40%; Table 5). As one might expect, the relative elevation and distance to channel of the abandoned alluvial ridge results in this region also remaining relatively dry (mean inundation frequency of 10%). In contrast, the central west backswamp experiences the highest maximum inundation frequency (98.43%), which is also where two pans are located. The area surrounding the current alluvial ridge, formed by the active channel, also experiences a high maximum of almost 51.97%.

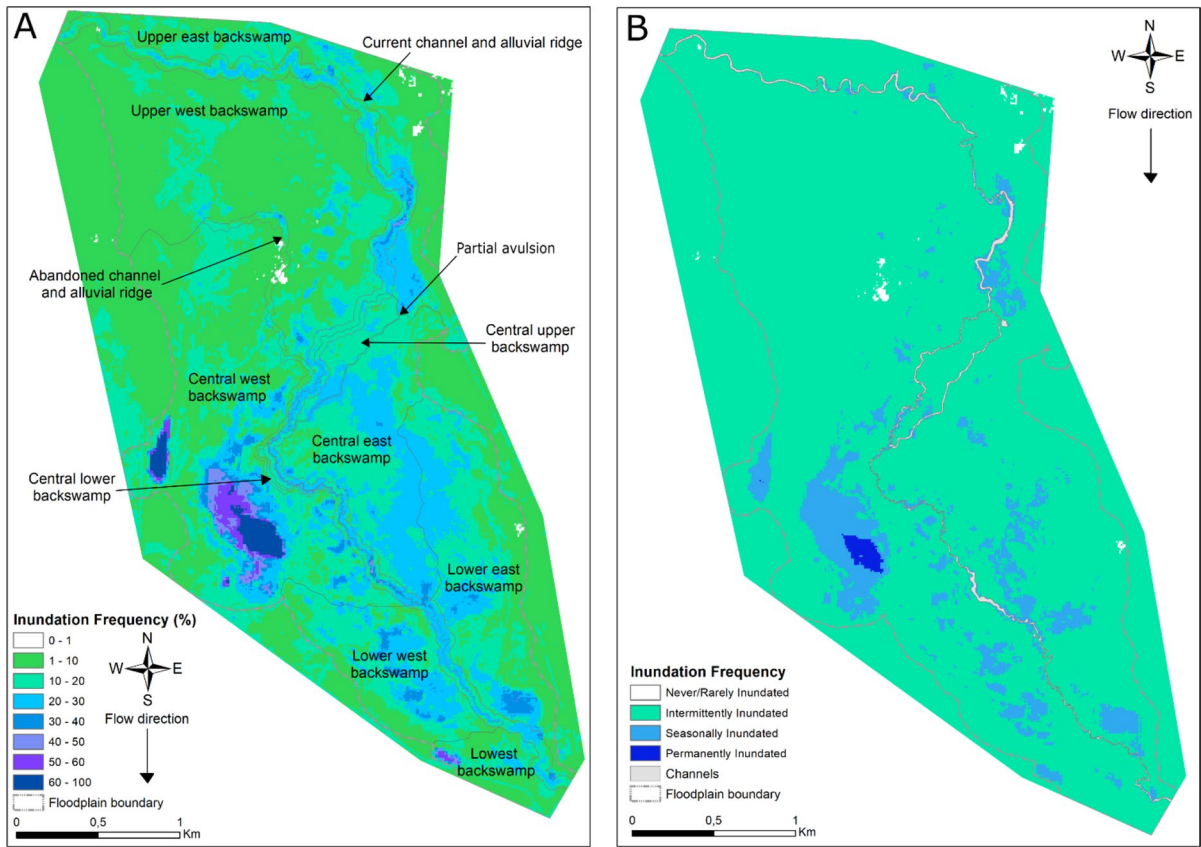


Fig. 4 **A** Inundation frequency (%) of the Nuwejaars River Floodplain, based on Sentinel imagery from 2018 to 2023, with the delineation of each macro-feature. **B** Inundation frequency represented according to hydroperiod classes (Ollis et al. 2013, 2015)

Table 4 Area (km²) and percentage of the floodplain extent (%) within each inundation frequency class according to Ollis et al. (2013, 2015)

Frequency of inundation	Inundation class	Inundation frequency (%)	Area (km ²)	% Area of floodplain
Less than a few days at a time	Never/rarely inundated	0–1%	0.02	0.20
Less than 3 months of a year	Intermittently inundated	1–25%	11.22	91.64
Inundated for 3 to 9 months of a year	Seasonally inundated	25–75%	0.96	7.82
Inundated more than 9 months of a year	Permanently inundated	75–100%	0.04	0.33

Discussion

Contemporary geomorphic processes in the Nuwejaars river floodplain

Meandering river floodplains are characterised by the lateral migration of the river channel and the interconnection of water, sediment and materials

between the floodplain surface and the river (Pereira et al. 2021). The Nuwejaars River is a non-perennial meandering river (Seaton et al. 2020). In meandering rivers, an alluvial ridge is typically produced by active channel aggradation, which results in the channel becoming more elevated than the adjacent floodplain (Grenfell et al. 2019), demonstrated by the maximum REM values of the current and

Table 5 Minimum, maximum, and mean inundation frequency (%) of macro-features, along with area and corresponding floodplain proportion. Macro-features are arranged from upstream to downstream

Macro-feature	Inundation Frequency			Area of feature (km ²)	Proportion of floodplain (%)
	Min (%)	Max (%)	Mean (%)		
Upper east backswamp	0.79	43.31	11.04	0.87	10.34
Upper west backswamp	0.79	33.86	8.40	1.92	22.74
Current channel and alluvial ridge	0.79	51.97	18.10	0.77	9.09
Abandoned channel and alluvial ridge	0.79	34.65	9.99	0.09	1.06
Central upper backswamp	5.51	29.13	17.45	0.15	1.78
Central west backswamp	0.79	98.43	17.37	2.00	23.69
Central east backswamp	2.36	44.09	18.28	0.89	10.58
Central lower backswamp	6.30	29.13	16.01	0.02	0.26
Lower east backswamp	0.79	42.52	15.35	1.01	11.97
Lower west backswamp	2.36	38.58	16.16	0.63	7.49
Lowest backswamp	2.36	59.06	11.54	0.30	3.52

abandoned channel's alluvial ridge reaching almost 5 m (Table 3), and seen in the cross sections in Fig. 3C. The relative elevation above the adjacent floodplain encourages overbank floodwater to flow into and become stagnant in neighbouring backswamps (Tooth et al. 2009). The formation of the alluvial ridge also promotes the opportunity for a channel avulsion (Ellery et al. 2011) and affects the distribution of water across the floodplain. For example, backswamp environments in the distal floodplain regions may be inundated more often than the alluvial ridge as a consequence of differences in elevation (Grenfell et al. 2019). This can be seen in Fig. 4A, where parts of the floodplain surface further away from the channel are inundated frequently.

As the Nuwejaars River flows into the floodplain system, it becomes narrower and reaches an avulsion just before the central upper backswamp (Fig. 3A). Avulsion in aggrading floodplains is typically associated with within-channel sedimentation which, over time, leads to both channel super-elevation and a reduction in the channel's gradient and capacity to carry flow (Slingerland and Smith 1998). During high flows, which occur relatively infrequently in dryland environments, discharge may exceed the channel's flow capacity, leading to water flowing over the channel banks. The relative elevation of the channel above the adjacent floodplain represents a gradient advantage (Lanzoni 2022) that promotes the redistribution

of water to distal floodplain environments and favours incision and the formation of a new channel (Ellery et al. 2011; Grenfell et al. 2009).

Avulsions that form a new channel through stages of sediment accumulation, deposition, and reworking are classified as progradational avulsions (Valenza et al. 2020), and typically result in a crevasse splay (e.g., Smith et al. 1989). In this case, the avulsion process is not yet complete as field observations indicate that both channels appear to convey some flow. The resulting feature does not conform to the typical morphology of a crevasse splay; it is well vegetated and is characterised by diffuse flow patterns. There is some minor aggradation visible at the proximal portion of the feature, as shown in cross-section 3 (Fig. 3C). Flow becomes concentrated with distance downstream, with a new channel properly developed by cross-section 5 and the full depth developed by cross-section 6 (Fig. 3C).

Hence, the region of the partial avulsion (consisting of the central upper and central east backswamps) has distinct hydrological conditions, and the inundation frequency of this region is relatively high. According to the hydroperiod determined in Fig. 4A, this region of the floodplain was, on average, inundated over 16% of the time between 2018 and 2023 (the partial avulsion region falls within the top sections of the central upper backswamp and central east backswamp; Fig. 3A). Additionally, water that moves as diffuse overland flow downstream of the avulsion

(within the central upper and central east backswamp) results in these central, eastern portions of the floodplain being inundated more regularly than other parts of the floodplain. The old course is located to the west of the avulsion and only conveys a portion of the total river flow during floods.

Hydroperiod modelling

The results of the hydroperiod analysis are considered minimum frequencies of inundation as there is potential for inundation to be under-represented due to vegetation cover (i.e., the growth of emergent vegetation is more prominent during the rainy season, Murray-Hudson et al. 2014) or cloud cover (i.e., although cloud cover percentage was limited, this resulted in fewer images being available for analysis, potentially reducing the number of 'wet' images). Future work could benefit from incorporating Synthetic Aperture Radar data, such as Sentinel-1, which can penetrate cloud cover and vegetation canopies, offering improved detection of inundation in areas where optical sensors may underestimate water presence.

Fig. 4A provides a high-resolution depiction of inundation frequency across the floodplain, while the hydroperiod classes in Fig. 4B, based on the national wetland classification system developed by Ollis et al. (2015), offer a more simplified and standardised framework for describing inundation regimes. This classification system is widely used in South Africa for wetland delineation and assessment, enhancing the comparability and applicability of the findings within a policy and conservation planning context. However, it is important to note that these broader classes do not fully capture the finer-scale variation in inundation frequencies present in Fig. 4A.

In the case of the Nuwejaars River Floodplain, the ecosystem mostly experiences intermittent inundation (91.64% of the floodplain area), with 7.82% of the floodplain experiencing seasonal inundation (Table 4; Fig. 4B). This drives dynamic variation in biophysical environments, with a diversity of terrestrial, semi-aquatic, and aquatic habitats represented (Pereira et al. 2021). The hydrological regime results in an inundation cycle that saturates the floodplain for different lengths of time, as seen in Fig. 4. During these cycles, the transition between terrestrial and aquatic zones varies. This variation is a key driver of vegetation patterns, ecological complexity, and

physical, chemical, and biological processes (Pereira et al. 2021), which all contribute to the range and quality of ecosystem service provision. Flooding and subsequent sedimentation facilitate numerous ecosystem services, such as soil nutrient exchange between the river channel and its associated floodplain (Kotze et al. 2009; Tsheboeng et al. 2014).

Based on the hydroperiod analysis over the five years, surface inundation is most prominent in the central and lower areas of the floodplain (Fig. 4A). The central east backswamp experiences the highest mean inundation frequency of 18.28% over the five years (Table 5). These lower-lying floodplain surface areas are gently sloping (Fig. 3), allowing ponding and water retention. Furthermore, as these areas experience diffuse flow due to being positioned downstream of the partial avulsion (see Fig. 3A), they are frequently saturated, and for longer durations. Additionally, areas proximal to the current channel are more likely to be more frequently inundated by channel overtopping. As the backswamps are positioned at a lower elevation due to the formation of the alluvial ridge (Table 3), they are potentially more susceptible to rapid active sedimentation.

On average, the upper west and east backswamps experience the lowest frequency of inundation (8.40 and 11.04% respectively; Table 5). As these regions occupy slightly higher elevation (second and third highest REM values; Table 3), they are expected to be less frequently inundated. Additionally, the abandoned channel and its alluvial ridge in this part of the system have received a low frequency of inundation over the five years (9.99%; Table 5). The majority of this abandoned channel is located far from the active channel in the upper western portion of the floodplain and typically does not receive any floodwaters.

The central west backswamp experiences the highest maximum inundation frequency (98.43%; Table 5), likely due to the two pans occurring in this region of the floodplain. The pans are located far from the active channels, suggesting that the high inundation frequencies observed here are likely not derived from flood waters, but rather from direct rainfall. The lowest backswamp has the subsequent highest maximum inundation frequency (59.06%; Table 5), which is likely accounted for by the artificial dam located on the floodplain's western border. The area surrounding the current alluvial ridge, formed by the active channel, also experiences a high maximum inundation

frequency of almost 51.97% (Table 5). This area surrounding the channel is inundated when the channel overtops its banks in periods of high flows.

Table 4 shows that 0.20% of the floodplain has never or rarely been inundated over the five years. These areas occur near the floodplain inlet, mainly in the upper-west backswamp. This portion of the floodplain is elevated slightly higher than the central and lower portions (Table 3), and the meandering river is confined to its course in this reach (see Fig. 3A). Additionally, these areas that correspond with ‘never inundated’ are generally located in areas that were historically disturbed by agriculture, also noticed by Amani et al. (2022). However, it could be that the satellite imagery does not detect inundation due to the method’s limitations and/or short duration of inundation in this area.

Effects of floodplain geomorphology on the hydroperiod

The hydroperiod of a floodplain, in combination with its geomorphological characteristics and processes, provide detailed insights into the spatial extent and degree of provision of ecosystem services, such as flood attenuation, nutrient assimilation, carbon sequestration, sediment trapping, and pollutant immobilisation (Acreman et al. 2007). Research considering floodplains tends to emphasise hydrological processes (Lisenby et al. 2019), and less attention has been given to geomorphic aspects (Lininger et al. 2019).

The geomorphic processes and geomorphology of the floodplain surface affect the spatial distribution of nutrients, organic matter, and pollutants because sediment and water preferentially accumulate in different positions within the landscape (Chaopricha and Marín-Spiotta 2014). Variation in flooding characteristics (inundation frequency and duration) within the floodplain, as well as within each macro-feature, is dependent on the morphology and structural arrangement of floodplain features. Although these macro-features were subdivided according to relative land surface elevation, sharp ecological boundaries do not separate them. Instead, gradual transitions exist. That the inundation characteristics of the features noticeably differ (Table 5) highlights the importance of each feature’s distinctive geomorphological attributes in contributing to the hydrological dynamics of the

floodplain ecosystem as a whole. The features’ physical properties, such as form, elevation, and area, were produced by specific geomorphic processes (Wheaton et al. 2015), and they consequently receive varying frequencies of inundation.

The shallow gradient (longitudinal slope of 0.05%; Fig. 3B) of the floodplain and the moderately low REM values of the portions of land surrounding the channel promote slow surface flows and retention of water in particular regions. Small increases in rainfall can lead to large proportions of a floodplain being flooded (Mertes 1997), which indicates the importance of the morphology of a floodplain in attenuating floods, retaining water and the sediment it carries. Furthermore, the geomorphic processes responsible for the occurrence of channel avulsion, the formation of abandoned channels, and aggradational features associated with avulsive processes are also significant in contributing to the floodplain’s ability to retain flood waters.

The geomorphic processes that lead to the occurrence of the avulsion (i.e., alluvial ridge aggradation and in-channel accretion rates leading to super-elevation of the channel above the floodplain), and the subsequent splay, are important in promoting diffuse flows and water retention in these regions. Avulsions play a key role in the distribution of water, sediment, and the materials the sediment carries, such as organic matter, nutrients, and contaminants across floodplains, “thereby influencing topography, substrate type, and hydroperiod, all of which have implications for ecological processes and patterns” (Larkin et al. 2016, p. 328). The combination of geomorphic and hydrologic processes occurring downstream of the partial avulsion controls the manner in which sediment and water are conveyed across the surface of the floodplain (Tooth et al. 2015). In addition to precipitation, the geomorphology of a floodplain and its catchment drive the floodplain’s inundation frequency, duration and magnitude (Pereira et al. 2021). This is evident by the incorporation of the HAND and slope layers into the hydroperiod model yielding a more rigorous hydroperiod result (Table 2). This demonstrates the significance that the underlying geomorphology of the floodplain has on the inundation regime.

Furthermore, the inclusion of multiple indices generally improved model performance. Combinations with only a few indices (e.g., 1, 2, 3) tended

to perform worse than those with more indices. The addition of topographic information (combination 7; Table 2) led to the highest overall accuracy, demonstrating the importance of terrain data in inundation mapping. Different indices capture various aspects of the landscape, and the results demonstrate the importance of combining multiple spectral indices for improved inundation mapping accuracy. Both the Revised Normalised Difference Water Index (RNDWI) and Modified Normalised Difference Water Index (MNDWI) appeared in many of the high-performing combinations, indicating their effectiveness in detecting water. By combining these indices, we were able to leverage their complementary strengths to improve the overall accuracy of inundation detection. In contrast to Wu et al. (2019), who confined the inundation frequency calculations to channel boundaries delineated by LiDAR-based depressions, we considered the entire floodplain area. This broader approach allows for a more comprehensive understanding of the floodplain dynamics, as well as allowing the geomorphology and topography of the floodplain to be incorporated into the analysis.

The highest accuracy achieved was 75.9% (Table 2), which, while good, suggests some limitations in the model's ability to detect inundation. The region of the partial avulsion, which we theoretically would have considered frequently inundated, was not characterised by the model as frequently inundated. As the model compares the satellite imagery's spectral characteristics with the JRC permanent water mask, the model only chooses a particular class with particular characteristics as being inundated. Therefore, pixels within this region are not characterised as having permanent water because there is typically emergent vegetation covering the area. As a result, it will not be recognised as fully inundated. The accuracy is thus likely lower due to the partial avulsion region failing to be characterised as frequently inundated because it is heavily vegetated and masks the appearance of surface water. Despite limited field samples, we utilised the available data to assess the model's accuracy against real-time, in-field observations.

A weakness of the approach presented is that it is not possible to distinguish between different drivers of inundation (river flood dispersal versus local rainfall). Floodplain inundation may be considered a process whereby water overtops the channel and

saturates the floodplain surface, or precipitation falls directly on a saturated surface. The satellite imagery is a representation of both processes; therefore, the hydroperiod map shows flood *retention* as a result of inundation after a flood (longer-term) and/or a rainfall event, and not the actual response to a river flood event (flood *extent*). However, the results still demonstrate a good representation of the floodplain's hydroperiod and provide meaningful information relevant to the research. Through further research that is beyond the scope of the current paper, we will integrate the current remote sensing approach with field flow measurements and hydrodynamic modelling, to advance understanding of the relative contributions of different flood water sources.

Conclusion

Developing the hybrid terrain–multispectral image model of the Nuwejaars River Floodplain's hydroperiod provided valuable information about the spatial and temporal variation in flood retention patterns and the frequency and duration of inundation in specific regions of the wetland. Incorporation of geomorphological and topographical data into the floodplain's hydroperiod model improved accuracy, precision, and recall statistics. The highest accuracy was achieved by including all Sentinel-2 bands, slope, HAND, NDVI, NDWI, RNDWI, MNDWI, and SNDWI, yielding an accuracy of 75.9% and a precision and recall of 66.7%. Additionally, integrating geomorphological insight into the analysis was critical for more meaningful interpretation of floodplain processes, which hydrological observations alone could provide. These broader integrated insights are necessary if we are to evaluate the implications of historical spatial variation and future changes in hydroperiod for floodplain ecological processes and ecosystem service provision.

This analysis also demonstrated the successful use of the LiDAR-derived DEM, remote sensing techniques, and geospatial computations to develop and visualise the Nuwejaars River Floodplain's morphology and structure. Macro-scale features were successfully identified, mapped and characterised based on their form and the processes that lead to their formation. The macro-features represent geomorphic subdivisions of the floodplain that may reflect different wetland processes and controls, due to their

differences in relative elevation, morphology, and topography. The topography and morphology of the floodplain surface aided in explaining the differences in the hydroperiod across the system, because inundation patterns are dependent on the surface area and morphology of the floodplain (Meyerhoff and Dehnhardt 2007).

Our findings illustrate the strong correlation between inundation frequency and floodplain geomorphology. The findings reveal how features such as partial avulsions and abandoned channels shape inundation patterns, offering valuable insights into floodplain dynamics. This underscores that geomorphology is not simply a backdrop for hydrological processes, but a primary driver that influences the spatial extent, timing, and duration of floodplain inundation. These insights are highly relevant for land-use planning, wetland conservation, and climate change mitigation strategies in similar semi-arid and anthropogenically influenced floodplain systems. Future work could benefit from incorporating Synthetic Aperture Radar data, such as Sentinel-1, and hydrodynamic modelling to improve hydroperiod model developments.

Acknowledgements We would like to sincerely thank the following people and organisations for their support: the Nuwejaars Wetlands Special Management Area for allowing us access to the floodplain; Mahima Vandayar's and Philip Myburgh's assistance in the field, the Stellenbosch Forestry Department for allowing us to use their laboratory facilities; the Stellenbosch Process Engineering Department and the Central Analytical Facility laboratories for their assistance with analyses; Geosmart for sharing the Stellenbosch University 5 m DEM with us, and the Council for Geoscience for sharing their geological data.

Author contributions S.M.A: Conceptualisation, Formal analysis, Investigation, Writing—Original draft, Writing—Review & editing, Visualisation, Project administration. Z.M: Conceptualisation, Methodology, Software, Validation, Formal analysis, Writing—Original draft, Supervision. M.G: Funding acquisition, Supervision, Writing—Review & editing. S.G: Conceptualisation, Writing—Review & editing, Supervision, Funding acquisition. All authors reviewed the manuscript.

Funding Open access funding provided by Stellenbosch University. This work is based on the research supported wholly by the National Research Foundation of South Africa (Grant Number: 136479, Reference Number: ESS210325590980). SMA was funded by the National Research Foundation and Stellenbosch University's Graduate School Turning the Tide Andrew W. Mellon Foundation scholarship.

Data availability No datasets were generated or analysed during the current study.

Declarations

Competing Interests Dr SE Grenfell serves on the Editorial board of Wetlands Ecology and Management.

Open Access This article is licensed under a Creative Commons Attribution 4.0 International License, which permits use, sharing, adaptation, distribution and reproduction in any medium or format, as long as you give appropriate credit to the original author(s) and the source, provide a link to the Creative Commons licence, and indicate if changes were made. The images or other third party material in this article are included in the article's Creative Commons licence, unless indicated otherwise in a credit line to the material. If material is not included in the article's Creative Commons licence and your intended use is not permitted by statutory regulation or exceeds the permitted use, you will need to obtain permission directly from the copyright holder. To view a copy of this licence, visit <http://creativecommons.org/licenses/by/4.0/>.

References

- Acreman MC, Fisher J, Stratford CJ, Mould DJ, Mountford JO (2007) Hydrological science and wetland restoration: some case studies from Europe. *Hydrol Earth Syst Sci* 11:158–169
- Amani M, Brisco B, Warren R, DeLancey ER, Seydi ST, Ponzos V (2022) Wetland hydroperiod analysis in Alberta using InSAR coherence data. *Remote Sens* 14:1–17. <https://doi.org/10.3390/rs14143469>
- Bickerton IB, Heydorn AEF, Grindley JR (1984) Estuaries of the cape: Part II: synopses of available information on individual systems. Council for Scientific and Industrial Research
- Campos JC, Sillero N, Brito JC (2012) Normalized difference water indexes have dissimilar performances in detecting seasonal and permanent water in the Sahara-Sahel transition zone. *J Hydrol* 464:438–446
- Cao RL, Li CJ, Liu LY, Wang JH, Yan GJ (2008) Extracting Miyun reservoir's water area and monitoring its change based on a revised normalized different water index. *Sci Surv Mapp* 33:158–160
- Chaopricha NT, Marín-Spiotta E (2014) Soil burial contributes to deep soil organic carbon storage. *Soil Biol Biochem* 69:251–264. <https://doi.org/10.1016/j.soilbio.2013.11.011>
- Ellery W, Grenfell M, Grenfell S, Kotze D, McCarthy TS, Tooth S, Grundling PL, Beckedahl H, Maitre DL, Ramsay L (2011) WET-origins: controls on the distribution and dynamics of wetlands in South Africa., WRC Report. Water Research Commission Report TT334/09, Pretoria
- Erasmus Z (2013) Status report on the agulhas plain study area. Cape Town
- Feyisa GL, Meilby H, Fensholt R, Proud SR (2014) Automated water extraction index: a new technique for surface water

- mapping using landsat imagery. *Remote Sens Environ* 140:23–35
- Foti R, del Jesus M, Rinaldo A, Rodriguez-Iturbe I (2012) Hydroperiod regime controls the organization of plant species in wetlands. *Proc Natl Acad Sci USA* 109:19596–19600. <https://doi.org/10.1073/pnas.1218056109>
- Frank E, Hall MA, Witten IH (2016) The WEKA Workbench. Online Appendix for data mining: practical machine learning tools and techniques
- Gao B-C (1996) NDWI—a normalized difference water index for remote sensing of vegetation liquid water from space. *Remote Sens Environ* 58:257–266
- Garousi-Nejad I, Tarboton DG, Aboutalebi M, Torres-Rua AF (2019) Terrain analysis enhancements to the height above nearest drainage flood inundation mapping method. *Water Resour Res* 55:7983–8009. <https://doi.org/10.1029/2019WR024837>
- Gordon N, García-Rodríguez F, Adams J (2012) Paleolimnology of a coastal lake on the Southern Cape coast of South Africa: sediment geochemistry and diatom distribution. *J African Earth Sci* 75:14–24. <https://doi.org/10.1016/j.jafrearsci.2012.06.008>
- Grenfell SE, Ellery WN, Grenfell MC (2009) Geomorphology and dynamics of the Mfolozi River floodplain, KwaZulu-Natal, South Africa. *Geomorphology* 107:226–240
- Grenfell S, Grenfell M, Ellery W, Job N, Walters D (2019) A genetic geomorphic classification system for southern African palustrine wetlands: global implications for the management of wetlands in drylands. *Front Environ Sci* 7:1–23. <https://doi.org/10.3389/fenvs.2019.00174>
- Han-Qiu XU (2005) A study on information extraction of water body with the modified normalized difference water index (MNDWI). *Natl Remote Sens Bull* 9:589–595
- Hua Y, Cui B, He W, Cai Y (2016) Identifying potential restoration areas of freshwater wetlands in a river delta. *Ecol Indic* 71:438–448
- Huang C, Peng Y, Lang M, Yeo I-Y, McCarty G (2014) Wetland inundation mapping and change monitoring using Landsat and airborne LiDAR data. *Remote Sens Environ* 141:231–242. <https://doi.org/10.1016/j.rse.2013.10.020>
- Jagganath T (2021) Understanding spatial patterns of dispersal and deposition of fine sediment and adsorbed phosphates in the Wiesdrift Wetland on the Nuwejaars River. University of the Western Cape, Bellville, Cape Agulhas
- Jin H, Huang C, Lang MW, Yeo I-Y, Stehman SV (2017) Monitoring of wetland inundation dynamics in the Delmarva Peninsula using Landsat time-series imagery from 1985 to 2011. *Remote Sens Environ* 190:26–41. <https://doi.org/10.1016/j.rse.2016.12.001>
- Khan SI, Hong Y, Wang J, Yilmaz KK, Gourley JJ, Adler RF, Brakenridge GR, Policelli F, Habib S, Irwin D (2011) Satellite remote sensing and hydrologic modeling for flood inundation mapping in lake Victoria basin: implications for hydrologic prediction in ungauged basins. *IEEE Trans Geosci Remote Sens* 49:85–95. <https://doi.org/10.1109/TGRS.2010.2057513>
- Khungwayo A (2022) Investigating the effects of nutrients and chlorophyll concentrations on the water quality of the Nuwejaars River, Cape Agulhas. University of the Western Cape, Bellville, Western Cape
- Kordelas GA, Manakos I, Aragonés D, Díaz-Delgado R, Bustamante J (2018) Fast and automatic data-driven thresholding for inundation mapping with sentinel-2 data. *Remote Sens* 10:1–23. <https://doi.org/10.3390/rs10060910>
- Kottek M, Grieser J, Beck C, Rudolf B, Rubel F (2006) World map of the Köppen-Geiger climate classification updated. *Meteorol Zeitschrift* 15:259–263. <https://doi.org/10.1127/0941-2948/2006/0130>
- Kotze D, Marneweck G, Batchelor A, Lindley D, Collins N (2009) WET-EcoServices: a technique for rapidly assessing ecosystem services supplied by wetlands
- Kraaij T, Hanekom N, Russell IA, Randall RM (2009) Agulhas national park state of knowledge. Cape Town
- Kulkarni A, Chong D, Batarseh FA (2020) Foundations of data imbalance and solutions for a data democracy. *Data democracy*. Elsevier, pp 83–106
- Lanzoni S (2022) Morphodynamic modeling of alluvial rivers and floodplains. *Treatise Geomorphol*. <https://doi.org/10.1016/B978-0-12-818234-5.00154-1>
- Larkin Z, Ralph T, Tooth S, Duller G, McCarthy T, Keen-Zebert A, Humphries M (2016) Implications of channel avulsion for the structure and functioning of semi-arid floodplain wetlands: examples from South Africa, in: INTECOL International Wetlands Conference (10th: 2016). International association for ecology (INTECOL), p 328
- Lefebvre G, Davranche A, Willm L, Campagna J, Redmond L, Merle C, Guelmami A, Poulin B (2019) Introducing WIW for detecting the presence of water in wetlands with landsat and sentinel satellites. *Remote Sens* 11:2210
- Lininger KB, Wohl E, Rose JR, Leisz SJ (2019) Significant floodplain soil organic carbon storage along a large high-latitude river and its tributaries. *Geophys Res Lett* 46:2121–2129. <https://doi.org/10.1029/2018GL080996>
- Lisenby PE, Tooth S, Ralph TJ (2019) Product vs. process? The role of geomorphology in wetland characterization. *Sci Total Environ* 663:980–991
- Liu HQ, Huete A (1995) A feedback based modification of the NDVI to minimize canopy background and atmospheric noise. *IEEE Trans Geosci Remote Sens* 33:457–465
- McCormack T, Campaña J, Naughton O (2023) Reconstructing flood level timeseries at seasonal wetlands in Ireland using Sentinel-1. *Remote Sens Environ* 299:113839. <https://doi.org/10.1016/j.rse.2023.113839>
- McFeeters SK (1996) The use of the normalized difference water index (NDWI) in the delineation of open water features. *Int J Remote Sens* 17:1425–1432. <https://doi.org/10.1080/01431169608948714>
- McLachlan A, Burns M (1992) Headland bypass dunes on the South African coast: 100 years of (mis)management. In: Carter RW (Ed.), *Coastal dunes: geomorphology, ecology and management for conservation: proceedings of the 3rd European dune congress galway, Ireland*, pp 71–79
- Mertes LAK (1997) Documentation and significance of the perirheic zone on inundated floodplains. *Water Resour Res* 33:1749–1762. <https://doi.org/10.1029/97WR00658>
- Meyerhoff J, Dehnhardt A (2007) The European water framework directive and economic valuation of wetlands: the restoration of floodplains along the river Elbe. *Eur Environ* 17:18–36. <https://doi.org/10.1002/eet.439>

- Mucina L, Rutherford MC (2006) The vegetation of South Africa, Lesotho and Swaziland. South African National Biodiversity Institute
- Murray-Hudson M, Wolski P, Cassidy L, Brown M, Thito K, Kashe K, Mosimanyana E (2014) Remote sensing-derived hydroperiod as a predictor of floodplain vegetation composition. *Wetl Ecol Manag* 23:1–14. <https://doi.org/10.1007/s11273-014-9340-z>
- Ollis DJ, Ewart-Smith JL, Day JA, Job NM, Macfarlane DM, Snaddon CD, Sieben EJJ, Dini JA, Mbona N (2015) The development of a classification system for inland aquatic ecosystems in South Africa. *Water SA* 41:727–745
- Ollis D, Snaddon K, Job N, Mbona N (2013) SANBI biodiversity series 22: classification system for wetlands and other aquatic ecosystems South Africa. Pretoria
- Pekel J-F, Cottam A, Gorelick N, Belward AS (2016) High-resolution mapping of global surface water and its long-term changes. *Nature* 540:418–422. <https://doi.org/10.1038/nature20584>
- Pena-Regueiro J, Sebastia-Frasquet MT, Estornell J, Aguilar-Maldonado JA (2020) Sentinel-2 application to the surface characterization of small water bodies in Wetlands. *Water (Switzerland)*. <https://doi.org/10.3390/w12051487>
- Pereira G, de Ramos RC, Rocha LC, Brunzell NA, Merino ER, Mataveli GAV, da Cardozo FS (2021) Rainfall patterns and geomorphological controls driving inundation frequency in tropical wetlands: How does the Pantanal flood? *Prog Phys Geogr Earth Environ* 45:669–686
- Privett SDJ, Krug RM, Forbes G, Gaertner M (2014) Wild flower harvesting on the Agulhas Plain, South Africa: Impact of harvesting intensity under a simulated commercial harvesting regime for two re-seeding and two re-sprouting fynbos species. *South African J Bot* 94:270–275. <https://doi.org/10.1016/j.sajb.2014.06.015>
- Qi J, Chehbouni A, Huete AR, Kerr YH, Sorooshian S (1994) A modified soil adjusted vegetation index. *Remote Sens Environ* 48:119–126. [https://doi.org/10.1016/0034-4257\(94\)90134-1](https://doi.org/10.1016/0034-4257(94)90134-1)
- Schulze R (1997) South African atlas of agrohydrology & climatology. Water Research Commission Report No TT82/96. Pretoria
- Seaton D, Dube T, Mazvimavi D (2020) Use of multi-temporal satellite data for monitoring pool surface areas occurring in non-perennial rivers in semi-arid environments of the Western Cape, South Africa. *ISPRS J Photogramm Remote Sens* 167:375–384. <https://doi.org/10.1016/J.ISPRSJPRS.2020.07.018>
- Slingerland R, Smith ND (1998) Necessary conditions for a meandering-river avulsion. *Geology* 26:435–438
- Smith LC (1997) Satellite remote sensing of river inundation area, stage, and discharge: a review. *Hydrol Process* 11:1427–1439
- Smith ND, Cross TA, Dufficy JP, Clough SR (1989) Anatomy of an avulsion. *Sedimentology* 36:1–23
- Tarboton DG (1997) A new method for the determination of flow directions and upslope areas in grid digital elevation models. *Water Resour Res* 33(2):309–319
- Thwaites RN (1987) Preliminary investigations into the geomorphological history of the Aghulas Plain. *South African Geogr J* 69:165–168
- Tockner K, Stanford JA (2002) Riverine flood plains: present state and future trends. *Environ Conserv* 29:308–330
- Tooth S, Rodnight H, McCarthy TS, Duller GAT, Grundling AT (2009) Late Quaternary dynamics of a South African floodplain wetland and the implications for assessing recent human impacts. *Geomorphology* 106:278–291. <https://doi.org/10.1016/j.geomorph.2008.11.009>
- Tooth S, Ellery W, Grenfell M, Thomas A, Kotze D, Ralph T (2015) 10 reasons why the geomorphology of wetlands is important. *Wetlands in Drylands Research Network*
- Trabucco A, Zomer RJ (2018) Global aridity index and potential evapotranspiration (ET0) climate database, *CGIAR Consortium for Spatial Information*, 2, <https://doi.org/10.6084/m9.figshare.7504448.v3>
- Tsheboeng G, Bonyongo M, Murray-Hudson M (2014) Flood variation and soil nutrient content in floodplain vegetation communities in the Okavango Delta. *S Afr J Sci*. <https://doi.org/10.1590/sajs.2014/20130168>
- Tucker CJ (1979) Red and photographic infrared linear combinations for monitoring vegetation. *Remote Sens Environ* 8:127–150
- Uhlemann SS, Sorensen JPR, House AR, Wilkinson PB, Roberts C, Gooddy DC, Binley AM, Chambers JE (2016) Integrated time-lapse geoelectrical imaging of wetland hydrological processes. *Water Resour Res* 52:1607–1625
- Valenza JM, Edmonds DA, Hwang T, Roy S (2020) Downstream changes in river avulsion style are related to channel morphology. *Nat Commun* 11:2116. <https://doi.org/10.1038/s41467-020-15859-9>
- van Deventer H, Linström A, Durand JF, Naidoo L, Cho MA (2022) Deriving the maximum extent and hydroperiod of open water from Sentinel-2 imagery for global sustainability and biodiversity reporting for wetlands. *Water SA* 48:75–89. <https://doi.org/10.17159/wsa/2022.v48.i1.3883>
- Wheaton JM, Fryirs KA, Brierley G, Bangen SG, Bouwes N, O'Brien G (2015) Geomorphic mapping and taxonomy of fluvial landforms. *Geomorphology* 248:273–295. <https://doi.org/10.1016/J.GEOMORPH.2015.07.010>
- Wu G, Liu Y (2014) Satellite-based detection of water surface variation in China's largest freshwater lake in response to hydro-climatic drought. *Int J Remote Sens* 35:4544–4558. <https://doi.org/10.1080/01431161.2014.916444>
- Wu G, Liu Y (2015) Capturing variations in inundation with satellite remote sensing in a morphologically complex, large lake. *J Hydrol* 523:14–23. <https://doi.org/10.1016/j.jhydrol.2015.01.048>
- Wu Q, Lane CR, Li X, Zhao K, Zhou Y, Clinton N, DeVries B, Golden HE, Lang MW (2019) Integrating LiDAR data and multi-temporal aerial imagery to map wetland inundation dynamics using google earth engine. *Remote Sens Environ* 228:1–13. <https://doi.org/10.1016/j.rse.2019.04.015>
- Xie Y, Sha Z, Yu M (2008) Remote sensing imagery in vegetation mapping: a review. *J Plant Ecol* 1:9–23. <https://doi.org/10.1093/jpe/rtn005>
- Xu H (2006) Modification of normalised difference water index (NDWI) to enhance open water features in remotely sensed imagery. *Int J Remote Sens* 27:3025–3033

Publisher's Note Springer Nature remains neutral with regard to jurisdictional claims in published maps and institutional affiliations.